Title

Simulation studies of a full-ring, CZT SPECT system for whole-body imaging of 99mTc and 177Lu

Journal

Medical Physics, 50(6)

ISSN

0094-2405

Authors

Huh, Yoonsuk

Caravaca, Javier

Kim, Jaehyuk

et al.

Publication Date

2023-06-01

DOI

10.1002/mp.16360

Peer reviewed

HHS Public Access

Author manuscript

Med Phys. Author manuscript; available in PMC 2023 September 15.

Published in final edited form as:

Med Phys. 2023 June ; 50(6): 3726–3737. doi:10.1002/mp.16360.

Simulation studies of a full-ring, CZT SPECT system for whole-body imaging of ^{99m}Tc and ^{177}Lu

Yoonsuk Huh[1,*], **Javier Caravaca**[1,*], **Jaehyuk Kim**[2], **Yonggang Cui**[3], **Qiu Huang**[4], **Grant Gullberg**[1,5], **Youngho Seo**[1,5,6,7,8]

[1]Department of Radiology and Biomedical Imaging, University of California, San Francisco, CA, USA

[2]Princess Margaret Cancer Centre, University Health Network, Toronto, ON, Canada

[3]Department of Nonproliferation and National Security, Brookhaven National Laboratory, Upton, NY, USA

[4]School of Biomedical Engineering, Shanghai Jiao Tong University, Shanghai, China

[5]Molecular Biophysics and Integrated Bioimaging Division, Lawrence Berkeley National Laboratory, Berkeley, CA, USA

[6]Department of Radiation Oncology, University of California, San Francisco, CA, USA

[7]Joint Graduate Group in Bioengineering, University of California, San Francisco and Berkeley, CA, USA

[8]Department of Nuclear Engineering, University of California, Berkeley, CA, USA

Abstract

Background—Single photon emission computed tomography (SPECT) is an imaging modality that has demonstrated its utility in a number of clinical indications. Despite this progress, a high sensitivity, high spatial resolution, multi-tracer SPECT with a large field of view suitable for whole-body imaging of a broad range of radiotracers for theranostics is not available.

Purpose—With the goal of filling this technological gap, we have designed a cadmium zinc telluride (CZT) full-ring SPECT scanner instrumented with a broad-energy tungsten collimator. The final purpose is to provide a multi-tracer solution for brain and whole-body imaging. Our static SPECT does not rely on the dual- and the triple-head rotational SPECT standard paradigm, enabling a larger effective area in each scan to increase the sensitivity. We provide a demonstration of the performance of our design using a realistic model of our detector with simulated body-sized phantoms filled with ^{99m}Tc and ^{177}Lu.

Corresponding authors contact: UCSF Physics Research Laboratory, Department of Radiology and Biomedical Imaging, University of California, San Francisco, California, 94143-0946, javier.caravacarodriguez@ucsf.edu, youngho.seo@ucsf.edu, Phone: (415) 353-9464.

*Co-first authors

Conflict of interest statement

The authors have no relevant conflicts of interest to disclose.

Methods—We create a realistic model of our detector by using a combination of a GATE Monte Carlo simulation and a finite element model for the CZT response, accounting for low-energy tail effects in CZT that affects the sensitivity and the scatter correction. We implement a modified dual-energy-window scatter correction adapted for CZT. Other corrections for attenuation, detector and collimator response, and detector gaps and edges are also included. The images are reconstructed using the maximum-likelihood expectation-maximization. Detector and reconstruction performance are characterized with point sources, Derenzo phantoms, and a body-sized National Electrical Manufacturers Association (NEMA) Image Quality (IQ) phantom for both ^{99m}Tc and ^{177}Lu.

Results—Our SPECT design can resolve 7.9 mm rods for ^{99m}Tc (140 keV) and 9.5 mm for ^{177}Lu (208 keV) in a hot-rod Derenzo phantom with a 3-minute exposure and reach an image contrast of 78% for ^{99m}Tc and 57% for ^{177}Lu using the NEMA IQ phantom with a 6-minute exposure. Our modified scatter correction shows an improved contrast-recovery ratio compared to a standard correction.

Conclusions—In this paper, we demonstrate the good performance of our design for whole-body imaging purposes. This adds to our previous demonstration of improved qualitative and quantitative ^{99m}Tc imaging of brain perfusion and ^{123}I imaging of dopamine transport with respect to state-of-the-art NaI dual-head cameras. We show that our design provides similar image quality and contrast to the commercial full-ring SPECT VERITON for ^{99m}Tc. Regarding ^{177}Lu imaging of the 208 keV emissions, our design provides similar contrast to that of other state-of-the-art SPECTs with a significant reduction in exposure. The high sensitivity and extended energy range up to 250 keV makes our SPECT design a promising alternative for clinical imaging and theranostics of emerging radionuclides.

Keywords

SPECT; CZT; full-ring; Monte Carlo simulation; finite element method

1. Introduction

Single photon emission computed tomography (SPECT) is a very important imaging modality in nuclear medicine. SPECT systems keep continuously evolving to improve their sensitivity, spatial resolution and image quality, and to enable access to emerging radionuclides by extending the gamma ray energy range.

One of the most recent technological breakthroughs is the adoption of the semiconductor cadmium zinc telluride (CZT) in SPECT systems [1], providing more compact detectors with higher energy resolution and a lighter weight [2–4]. Another important advance is the substitution of the standard dual- or triple-head SPECT rotating around the subject, by a semi-stationary and multi-headed ring geometry in which each head independently moves forward and backward to get practically in contact with the subject, with an additional swiveling motion to allow each head to face the subject and reduce the number of unused detector parts (VERITON [5]). This design was lately adopted by another commercial SPECT/CT system (GE StarGuide [6]).

In [7], we proposed a full-ring CZT SPECT system with variable aperture, i.e., with detectors that can move in the radial direction in order to accommodate the detectors as close as possible to the subject. This design featured the addition of parallel-hole tungsten collimators designed in-house for a good performance in the 100 keV to 250 keV energy range [8]. The main organ-specific clinical applications that we targeted were ^{99m}Tc-based brain perfusion [9] and ^{123}I-based dopamine transporter imaging [10], showing that our system can improve sensitivity and reduce the acquisition time with equivalent contrast-to-noise ratio (CNR) and spatial resolution compared to conventional two-headed NaI-based SPECT systems.

In this paper, we further explore the performance of our design by evaluating it for whole-body imaging purposes with the standard ^{99m}Tc, and with the promising theranostics isotope ^{177}Lu. Our goal is to prove that our design can provide a multi-purpose solution for a number of clinical cases such as whole-body ^{99m}Tc imaging for metastatic cancer as well as ^{177}Lu imaging during radiotherapy treatment of gastroenteropancreatic neuroendocrine tumors [11] and metastatic-castration-resistant prostate cancer [12]. Our detector model is improved with respect to [7] by including a realistic CZT response based on a finite element method (FEM [13]). To adapt our approach to whole-body imaging, we add an energy-window-based scatter correction [14]. Finally, we characterize the detector's performance with Derenzo phantoms and a National Electrical Manufacturers Association (NEMA) Image Quality (IQ) phantom.

The paper is structured in the following way: Sec. 2 describes the detector geometry, simulation framework, image reconstruction and correction methods, and defines figure-of-merits used in our characterization. Sec. 3 reports the predicted performance of our system, namely, the sensitivity, image quality and contrast. Sec. 4 discusses the results comparing them with the literature, and Sec. 5 concludes.

2. Materials and methods

In this section we describe the detector's design, our Monte Carlo simulation, including the FEM model, and present our image reconstruction approach, including generation of the projections and the implementation of the corrections (see Fig. 1 for an overview of the analysis flow).

2.1 System and phantom geometries

Our design is composed by eight independently movable and swiveling detector heads arranged in a full-ring configuration (Fig. 2). Each head has a 179.2 mm × 128 mm detector surface with 1.6 mm × 1.6 mm pixels of 5-mm thickness. Each head has the ability to swivel as shown in Fig. 2. The detector heads are located at 240 mm radius around the center of the imaging region, which is further than in our previous brain imaging simulation study [7] in order to accommodate a human torso. Given the further distance, the heads are oriented such that their shorter size are parallel to the Z axis, as opposed to our previous study. In this way, we cover a larger angular region than in our previous brain experiment. This configuration corresponds to the closest that the detector heads can be from the center and from each other

without preventing them to freely swivel. Table I summarizes our system specifications and compares them to the published parameters of the VERITON system [5].

The simulated geometries of the Derenzo and NEMA IQ phantoms along with their specifications are shown in Fig. 3. The Derenzo phantom is a 108-mm radius plastic cylinder that contains six groups of rods of 88 mm length of different diameters (19.1 mm, 12.7 mm, 11.1 mm, 9.5 mm, 7.9 mm, 6.4 mm), which are greater than in our previous brain study [7]. Two different Derenzo phantoms are simulated: a hot-rod phantom and a cold-rod phantom. The inactive material (rods for the cold-rod phantom and main body of the phantom for the hot-rod one) was simulated as polyethylene while the aqueous radioactive solution (contained in the rods for the hot-rod and in the main cavity for the cold-rod) was simulated as water. The NEMA IQ phantom was simulated as a polyethylene phantom filled with water (warm region) and polyethylene spheric shells filled with water (hot region). The volume between the phantoms and the detector heads was simulated as air.

2.2 Simulation model

Achieving an accurate detector simulation is crucial for the detector design phase. It has been shown that the charge transport, trapping and diffusion, affect the charge induction efficiency (CIE), charge sharing between pixels, and crosstalk in CZT. These effects introduce important features in the energy spectra, namely, a low-energy tail which reduces sensitivity, and a contamination of the photopeak energy window with scattered photons, which reduces image contrast and quantification accuracy [16–18]. Hence, the simulation of this effect is crucial for an accurate detector model. Models based on a FEM have been successfully developed and validated in [13, 16, 18], following the method suggested in [19, 20].

To simulate our detector, we followed an approach similar to the one in [13], in which a detector model based on GATE Monte Carlo (MC) simulations and a COMSOL MULTIPHYSICS FEM implementation is adopted. This model is the one used in our analysis to produce a more accurate detector response and more realistic images.

2.2.1 Monte Carlo simulation—We used the Geant4 Application for Tomographic Emission (GATE) [21] to simulate gamma ray propagation in the subject and detector. The particle transport was modelled by the *emstandard_opt4* model, which uses the *G4LivermorePhotoelectricMode* and *G4RayleighScattering* Geant4 models that provide a high accuracy simulation of electrons and ion tracking. We added the *RadioactiveDecay* Geant4 process in order to model radionuclide gamma ray emissions with the correct energy and branching ratio for ^{99m}Tc and ^{177}Lu.

For the CZT detector, we simulated the commercial M1085 CZT module from Redlen with a 1.6 mm pixel pitch array of 16×16 and 5-mm thickness. CZT material region was defined as sensitive detectors in GATE to store the information of the energy depositions. The tracking information of each photon was recorded in ROOT format indexed by run, event, detector and pixel, as well as the deposited energy values and their local positions in the pixel. Inter-crystal scattered photons were identified by hits generated in the same event but at different detector and pixel index numbers. An energy resolution of 6.5% full width at half

maximum (FWHM) for CZT, as reported for the M1085 from Redlen, was simulated as a Gaussian smearing of the deposited energy value provided by GATE.

2.2.2 Finite element model—The number of generated charge carriers (electron and hole pairs) in CZT is proportional to the deposited energy. These carriers need to drift towards the anode or the cathode to be detected. This process is affected by the charge transport, trapping and diffusion [16], which yields a position-dependent charge induction efficiency (CIE) that needs to be accounted for in order to obtain a realistic CZT detector response.

In [7] we approximated this effect by a simple inefficiency factor of 65%. For this study, we followed the more sophisticated method described in [13]. We estimated the CIE using the adjoint electron n* continuity equation suggested in [19, 20]

$$\frac{\partial n^*}{\partial t} = \mu_e \nabla \varphi \nabla \phi_w - \frac{n^*}{\tau_e} + \mu_e \nabla \varphi \nabla n^* + D_n \nabla^2 n^*, \quad (1)$$

where φ is the electric potential, μ_e is the mobility of the electrons, ϕ_w is the weighting potential, τ_e is the average lifetime of the electrons, and D_n is the diffusion constant for electrons. The value of φ can be obtained by solving the Laplace equation,

$$\nabla^2 \varphi = 0. \quad (2)$$

Both holes and electrons are considered.

The charge transport model was implemented in the COMSOL MULTIPHYSICS software and equation (1) solved with the FEM model. We considered a 3 pixel × 3 pixel detector module with the same pixel size corresponding to our MC model. The required material property parameters were acquired from the specifications of the CZT detector M1085 from REDLEN (Table II).

Three 3D CIE maps were obtained by solving Eq. (1) for three-pixel positions: center, side and edge. Fig. 4a shows the CIE map for the center pixel. The small-pixel effect [22] is clearly observed in Fig. 4b for the CIE curves as a function of interaction depth for center, edge, and side pixels at the nominal −500V voltage. The curves are averaged over the X and Y dimensions. For simplicity and given the very small differences, we used the CIE obtained with the center pixel to model all the pixels in our detector.

The effect of CIE in the energy spectrum is illustrated in Fig. 5 for a ^{99m}Tc point source at the center of the detector (defined in Fig. 2). The CIE decreases the number of counts in the photopeak region by approximately 70% and increases the contribution of primary photons to the low-energy tail. The bump between 100 keV and 125 keV is due to the scattered gamma-rays. This is only obvious for the case without CIE (red curve in Fig. 5) due to the smearing introduced by CIE (blue curve). The detector model including CIE (blue curve) is the one used to generate the projections, implement the scatter correction, and produce the simulated data for the imaging performance studies.

2.3. Extended projections and gap and edge corrections

A detector full swiveling motion from −42.5° to 42.5° in 18 steps of 5° was simulated for all the cases. We collect counts in the photopeak region, defined for ^{99m}Tc as a window centered in 140.5 keV with a 6% width (131 keV to 149 keV), and for ^{177}Lu as a window centered around 208 keV with a 10% width (187 keV to 229 keV). Only the highest energy peak was included in this analysis.

In order to mitigate the effect of the limited field of view of each individual detector head, we concatenate the views of adjacent detector heads to generate extended projections of 224 × 80 pixels total. This results in 72 extended projections. These extended projections present gaps between two adjacent detectors which affects the final image quality. This was corrected for by shifting the center of the extended projection (gap correction), whose full mathematical formulation and performance are detailed in [7]. Another artifact introduced in the extended projection is the truncation of the edges of the subject when these are outside the view of the detector heads. This was corrected for by linearly extrapolating the extended projections to recover the edges of the subject (edge correction). Detailed derivation of this correction can also be found in [7].

2.4. Scatter correction

The extended projections were corrected by the photons scattered in the subject by using an energy window method [23]. A major consequence of the low-energy tail in CZT is that it complicates energy window-based scatter correction methods since the contamination of photopeak events in the low-energy tail leads to an overcorrection [24]. A standard dual-energy-window (DEW) scatter correction was successfully adapted for CZT by modeling the CZT low-energy tail with using data-driven approaches in [14, 24] and MC-driven approaches in [17, 25].

In this study, we compared two different DEW scatter correction methods: one with a typical DEW method (DEW) and another modified DEW that includes a low-energy tail correction for CZT (mDEW). The DEW method assumes that the number of scattered photons inside the photopeak window used for the projections can be estimated from the number of scattered photons in a lower energy window [23]. Then, for pixel j of a given projection

$$n_{PM}^{j} = n_{PE}^{j} + n_{S}^{j} = n_{PE}^{j} + k\, n_{SM}^{j} \tag{3}$$

where n_{PM}^{j} is the total number of events measured in the photopeak window, n_{PE}^{j} is the number of primary photons (photoelectric interactions) in the photopeak window, n_{S}^{j} is the number of scattered photons in the photopeak window, n_{SM}^{j} is the total number of events measured in a low-energy window, and k is a factor that needs to be modeled or determined empirically. We used the typical value $k = 0.5$ [23]. For DEW, we consider a scatter window from the low edge of the photopeak window down to 122 keV for ^{99m}Tc and to 166 keV for ^{177}Lu (Fig. 6).

The mDEW considers that the low-energy window is also populated by primary photons with a low CIE [14, 24], so Eq. (3) is modified to:

$$n_{PM}^{j} = n_{PE}^{j} + k_m\left(n_{SM}^{j} - m\, n_{PE}^{j}\right) \Rightarrow n_{PE}^{j} = \frac{n_{PM}^{j} - k_m n_{SM}^{j}}{1 - k_m m} \quad (4)$$

where k_m and m are calibrated following the methods described in [14]. m characterizes the low-energy tail in CZT and it is calculated as the ratio of events in the scatter region, P_{SW}, divided by those in the photopeak region, P_{PE}, for a point source in air:

$$m = P_{SW}/P_{PE} \quad (5)$$

k_m represents the ratio between the scatter events in the photopeak, S_{PE}, divided by the scatter events in the scatter window, S_{SW}:

$$k_m = S_{PE}/S_{SW} \quad (6)$$

S_{PE} is estimated as the difference in number of events in the photopeak window between the phantom and a point source. We used an 8:1 ratio for ^{99m}Tc (80 kBq/mL in the hot spheres and 10 kBq/mL in the warm background) as recommended by NEMA for ^{99m}Tc [26], and a higher 12:1 ratio for ^{177}Lu (120 kBq/mL versus 10 kBq/mL) as in [27]. For mDEW, we extended the scatter windows to 110 keV for ^{99m}Tc and to 137 keV for ^{177}Lu (Fig. 6). The larger scatter window helped selecting more true scatter events which results in a better estimation of the scatter fraction.

For DEW and mDEW, the estimated scatter fraction was subtracted from the projection data, which was subsequently fed into the reconstruction algorithm STIR.

2.5. Image reconstruction

The series of 2D extended projections was reconstructed using the maximum likelihood expectation maximization (MLEM) method [28] implemented in the software for tomographic image reconstruction (STIR) package [29, 30]. This package has built-in corrections for gamma ray attenuation, and collimator and detector response. The output image size was 224 × 224 × 80 with a 1.6 mm voxel size, and the number of iterations for MLEM reconstructions was optimized case by case.

2.6. Sensitivity calculation

We defined the total sensitivity, S, of our system, and the sensitivity to selected counts, S', as:

$$S = \frac{C}{T \times A}, \quad S' = \frac{C'}{T \times A}, \quad (7)$$

where C is the number of detected counts independent of the energy, C' is the number of selected counts in the photopeak region, T is the time in seconds, and A is the total activity of the subject. The sensitivities were calculated for two cases: for a point source placed in air at the center of the detector (Fig. 2a), and for a hot-rod Derenzo phantom to estimate the impact of the attenuation.

2.7. Image quality with Derenzo phantoms

Two types of Derenzo phantoms (hot-rod and cold-rod, Fig. 3a) were used to assess the image quality by reconstructing images. The hot-rod phantom has a rod activity concentration of 300 kBq/mL for ^{99m}Tc and 550 kBq/mL for ^{177}Lu. The cold-rod phantom contains a total activity of 175 MBq of ^{99m}Tc as in [5]. We simulate the hot-rod phantom at the center of the detector for an exposure of 10 s/step, for a total exposure of 3 minutes. The cold-rod phantom is simulated for total exposures of 3, 9, 18 and 30 minutes. We perform 300 MLEM iterations. The final images implement all the corrections described previously. The hot-rod images correspond to the sum over the length of the phantom (88 mm or 55 slices) with a 2-pixels width 2D gaussian filter, and the cold-rod phantoms images corresponds to a 5-mm transaxial slice with no further processing.

2.8. Image contrast with NEMA IQ phantom

The image contrast was measured using the NEMA IQ phantom (Fig. 3b). The sphere activity concentrations were 80 kBq/mL for ^{99m}Tc and 120 kBq/mL for ^{177}Lu, placed in a warm background of 10 kBq/mL for both isotopes. The impact of the scatter corrections was studied by reconstructing images with either no scatter correction, DEW, or mDEW, for ^{99m}Tc and ^{177}Lu. The images were postprocessed using a 3D Gaussian filter of 1-pixel width. We quantitatively assessed the image quality by calculating the contrast recovery coefficient (CRC) for each of the six spheres, following the NEMA standard NU2–2007 recommendation, as

$$CRC = \frac{M_{sphere}/M_{bg} - 1}{R_{sphere}/R_{bg} - 1}, \tag{8}$$

where M_{sphere} and M_{bg} are the average activity concentrations in the region of interest (ROI) and R_{sphere} and R_{bg} are the true activity concentrations inside the spheres and in the warm background, respectively. Only the central slice was considered following the NEMA standard NU2–2007. ROIs were chosen as circular regions centered in each corresponding sphere and with a radius equal to the radius of the sphere. The background ROI was composed of twelve circular regions around the warm background with a radius equivalent to the largest sphere.

3. Results

3.1. mDEW calibration

For ^{99m}Tc, the values of k_m and m are 0.264 and 0.096, respectively, and for ^{177}Lu the values are 0.05 and 0.438, respectively (Fig. 6).

3.2. Sensitivity

Sensitivities, as defined in Eq. 6, are shown in Table III for point sources at the center and for the hot-rod Derenzo phantom, for ^{99m}Tc and ^{177}Lu. Sensitivity is lower for ^{177}Lu due to the lower branching ratio and the higher energy of the gamma-rays, which have a lower photoelectric cross-section. The ratio between the sensitivity with the phantom and with

the point source is 0.40 for ^{99m}Tc and 0.46 for ^{177}Lu, lower than unity due to gamma-ray attenuation in the object.

3.3. Image quality

The hot-rod Derenzo phantom images for ^{99m}Tc and ^{177}Lu after 300 MLEM iterations are shown in Fig. 7. The smallest rods that can be resolved are the outer row of the 7.9-mm diameter rods with a peak-to-valley ratio of 1.67 for ^{99m}Tc, and the 9.5-mm diameter with a peak-to-valley ratio of 1.9 for ^{177}Lu. The image quality is worse towards the center of the phantom. In Fig. 7, we also compared the profiles for the smallest resolvable rod for different MLEM iterations. The peak-to-valley ratio does not significantly change after 300 iterations.

The effect of the gap and edge corrections can be observed in Fig. 8, where images of the Derenzo phantom filled with ^{99m}Tc are shown. To better illustrate the effect of each correction, the difference between images with and without corrections are also shown.

The reconstructed transaxial slices for the cold-rod Derenzo phantom are shown in Fig. 9 for the different exposures. Higher noise can be appreciated for lower exposures. The rods of 7.9 mm diameter are partially visible while the 6.4-mm are hardly resolved.

3.4 Image contrast

Figure 10 shows the reconstructed images of the NEMA IQ phantom images without scatter correction and with DEW and mDEW corrections for ^{99m}Tc and ^{177}Lu. The application of mDEW results in a slight increase of noise compared to the others due to the subtraction of true counts detected in the low-energy tail.

The CRC as a function of the sphere diameter with and without scatter correction is presented in Fig. 11. Including a scatter correction improves the CRC, as expected. The impact of the DEW correction is greater for ^{177}Lu than for ^{99m}Tc. mDEW improves CRC with respect to the typical DEW.

4. Discussion

This study continues our work published in [7] by demonstrating in simulation that our design performs well at different energies relevant for clinical purposes (140 keV with ^{99m}Tc and 208 keV with ^{177}Lu). We also expand the scope of our design from brain imaging to whole-body imaging applications. Furthermore, we have improved our CZT model with a FEM, and implemented a new mDEW scatter correction.

Our simulation study shows an image quality similar to that of VERITON CZT SPECT [5] for ^{99m}Tc phantoms, with the 7.9-mm cold-rods of the Derenzo phantom being partially visible. The image quality between 9- and 30-minutes exposure are very similar, suggesting that the exposure can be reduced by a factor of 3 without significant loss of image quality. The sensitivity of our system calculated with a point source in air is 425.0 ± 4.9 counts/s/MBq. This is larger than that achieved by VERITON when not in focus mode (236.68 counts/s/MBq). Our system also allows a focus mode, but we have not performed further

investigation on that particular configuration. The sensitivity is calculated at a radius of rotation of 24 cm versus 15 cm due to the fact that our detector heads cannot get closer to the center in the current configuration. Nevertheless, the effect of the radius of rotation on the sensitivity should be small. The contrast obtained with the NEMA IQ is not directly comparable to that reported for VERITON since cold spheres are used in their studies and a different CRC expression is employed. As opposed to VERITON, our results with ^{99m}Tc still need to be validated by an experimental setup.

The imaging of ^{177}Lu phantoms demonstrates that our system is capable of reconstruction of ^{177}Lu images with reasonable quality and CRC at low exposures. Since no quantitative imaging of ^{177}Lu with VERITON has been reported in the literature, we compare it to [27], which uses the Discovery 670 CZT system, a dual-head CZT SPECT/CT with a rotating gantry. Our design reaches a similar CRC for the imaging of the 208 keV gamma-ray line for an exposure of only 6 minutes with an activity of 550 kBq/mL. For a hot-rod Derenzo phantom, our sensitivity is 14.0 ± 0.7 counts/s/MBq, compared to the sensitivity of 6.7 counts/s/MBq of the Discovery 670 CZT computed with a NEMA IQ phantom. Again, our ^{177}Lu results need to be experimentally validated. A recent study of ^{177}Lu imaging with the GE StarGuide [6] shows comparable CRC to the ones we report.

Our design provides a finer axial slice by ~1.5 times (1.6mm vs. 2.5mm). However, the larger axial length of VERITON (315 mm) with respect to our design (128 mm) reduces the number of axial steps needed for full-body scans by a factor of ~2.5. VERITON requires ~5 bed positions for a full-body ^{99m}Tc scan, while we would require ~12. This compensates the potential decrease in exposure by a factor three described above, so the resulting whole-body image exposure would be similar to that of VERITON. We could further improve the performance of our approach by optimizing the swiveling angle and the exposure per step, but we have not explored that option for the current study.

As discussed, the main goal of this design is to extend the energy range of good performance of SPECT/CT (typically lower than 200 keV) in order to efficiently image the 208 keV ^{177}Lu gamma-ray. This gamma-ray line shows a higher branching ratio (11%) than that of the lower-energy 113 keV (6%), and less gamma-ray attenuation, so it has been shown to be more desirable for imaging purposes [31]. A promising progress towards ^{177}Lu imaging has been recently presented in [6]. We have not performed studies with other relevant isotopes emitting beyond 208 keV such as ^{223}Ra (~80 keV, 154 keV and 269 keV, or 271 keV from its short-lived ^{219}Rn daughter) or ^{131}I (364 keV and 637 keV). The capability of our system to image those isotopes needs to be evaluated in dedicated studies, although the imaging performance of higher energy gamma-rays will likely be degraded. A way to improve spatial resolution and image quality could be to combine our system with a dual-layer collimator concept, as presented in [15].

Given the larger subject size, a scatter correction becomes much more relevant in the current work than in our previous organ-specific studies [7]. The mDEW scatter correction shows a good performance for ^{99m}Tc and ^{177}Lu, but more sophisticated methods will be necessary to account for the low-energy tail when more than one gamma-ray is present, like for the low

energy ^{177}Lu emission or in a multi-tracer imaging scenario. MC-based models could solve this issue [17, 25].

The CIE obtained with the FEM method used to simulate the small-pixel effect in CZT is compared to that in the literature [13]. Although the pixel pitch and depth are slightly different, an equivalent response is found – the CIE increases as we get further from the anode, plateauing at 2 mm to a value close to 90%. The similarity of the results indicates that the prediction of our model is reasonable.

5. Conclusion

In this paper, we proposed a non-rotating CZT SPECT detector with dedicated tungsten collimators to extend the energy range to 250 keV. Its performance is reported for whole-body imaging using phantoms with ^{99m}Tc and ^{177}Lu. The predicted sensitivity doubles that of state-of-the-art systems for both isotopes, resulting in quality images with short exposures. For ^{99m}Tc, we can partially resolve the 7.9 mm rods in a hot-rod and cold-rod Derenzo phantom, and obtain a CRC larger than 50% for spheres with a diameter larger than 17 mm in a NEMA IQ phantom. For ^{177}Lu, we can partially resolve the 7.9 mm rods of the Derenzo phantom in 3 minutes using the higher-energy gamma-ray emission (208 keV), and obtain a CRC larger than 50% in 6 minutes for spheres with a diameter larger than 28 mm in a NEMA IQ phantom. This is a relevant result for the imaging of emerging radionuclides and for theranostics.

Acknowledgments

This work was supported in part by National Institute of Biomedical Imaging and Bioengineering under grants R01EB026331 and R01EB012965, National Heart, Lung, and Blood Institute under grant R01HL135490.

References

1. Van den Wyngaert T, et al. , SPECT/CT: Standing on the Shoulders of Giants, It Is Time to Reach for the Sky! Journal of Nuclear Medicine, 2020. 61(9): p. 1284–1291. [PubMed: 32620702]
2. Imbert L, et al. , A one-shot whole-body bone SPECT may be recorded in less than 20 minutes with the high-sensitivity Veriton® CZT-camera. Journal of Nuclear Medicine, 2019. 60(supplement 1): p. 1288–1288.
3. Lee JS, et al. , Advances in imaging instrumentation for nuclear cardiology. J Nucl Cardiol, 2019. 26(2): p. 543–556. [PubMed: 28718074]
4. Goshen E, et al. , Feasibility study of a novel general purpose CZT-based digital SPECT camera: initial clinical results. EJNMMI Phys, 2018. 5(1): p. 6. [PubMed: 29536291]
5. Desmonts C, et al. , Evaluation of a new multipurpose whole-body CzT-based camera: comparison with a dual-head Anger camera and first clinical images. EJNMMI Phys, 2020. 7(1): p. 18. [PubMed: 32185566]
6. Ferri V, Zananiri R, and Iagaru A, Performance evaluation of a novel multi-detector CZT-based SPECT/CT system using Tc99m and Lu177. 2022, Soc Nuclear Med.
7. Huh Y, et al. , Evaluation of a variable-aperture full-ring SPECT system using large-area pixelated CZT modules: A simulation study for brain SPECT applications. Medical Physics, 2021. 48(5): p. 2301–2314. [PubMed: 33704793]
8. Weng F, et al. , An energy-optimized collimator design for a CZT-based SPECT camera. Nucl Instrum Methods Phys Res A, 2016. 806: p. 330–339. [PubMed: 26640308]

9. Hirao K, et al. , The prediction of rapid conversion to Alzheimer's disease in mild cognitive impairment using regional cerebral blood flow SPECT. Neuroimage, 2005. 28(4): p. 1014–1021. [PubMed: 16129627]
10. Neumeyer JL, et al. , N-Omega-Fluoroalkyl Analogs of (1r)-2-Beta-Carbomethoxy-3-Beta-(4-Iodophenyl)-Tropane (Beta-Cit) - Radiotracers for Positron Emission Tomography and Single-Photon Emission Computed-Tomography Imaging of Dopamine Transporters. Journal of Medicinal Chemistry, 1994. 37(11): p. 1558–1561. [PubMed: 8201589]
11. Strosberg J, et al. , Phase 3 Trial of (177)Lu-Dotatate for Midgut Neuroendocrine Tumors. N Engl J Med, 2017. 376(2): p. 125–135. [PubMed: 28076709]
12. Fendler WP, et al. , (177)Lu-PSMA Radioligand Therapy for Prostate Cancer. J Nucl Med, 2017. 58(8): p. 1196–1200. [PubMed: 28663195]
13. Myronakis ME and Darambara DG, Monte Carlo investigation of charge-transport effects on energy resolution and detection efficiency of pixelated CZT detectors for SPECT/PET applications. Medical Physics, 2011. 38(1): p. 455–467. [PubMed: 21361214]
14. Mann S and Tornai M, Initial evaluation of a modified dual-energy window scatter correction method for CZT-based gamma cameras for breast SPECT. SPIE Medical Imaging. Vol. 9413. 2015: SPIE.
15. Boutaghane N, et al. , Dual-layer collimator for improved spatial resolution in SPECT with CZT camera: an analytical and Monte Carlo study. Phys Med Biol, 2022. 67(6).
16. Bolotnikov AE, et al. , Te Inclusions in CZT Detectors: New Method for Correcting Their Adverse Effects. Ieee Transactions on Nuclear Science, 2010. 57(2): p. 910–919.
17. Holstensson M, et al. , Model-based correction for scatter and tailing effects in simultaneous 99mTc and 123I imaging for a CdZnTe cardiac SPECT camera. Phys Med Biol, 2015. 60(8): p. 3045–63. [PubMed: 25803643]
18. Guerra P, Santos A, and Darambara DG, Development of a simplified simulation model for performance characterization of a pixellated CdZnTe multimodality imaging system. Physics in Medicine and Biology, 2008. 53(4): p. 1099–1113. [PubMed: 18263961]
19. Prettyman TH, Method for mapping charge pulses in semiconductor radiation detectors. Nuclear Instruments & Methods in Physics Research Section a-Accelerators Spectrometers Detectors and Associated Equipment, 1999. 422(1–3): p. 232–237.
20. Prettyman TH, Theoretical framework for mapping pulse shapes in semiconductor radiation detectors. Nuclear Instruments & Methods in Physics Research Section a-Accelerators Spectrometers Detectors and Associated Equipment, 1999. 428(1): p. 72–80.
21. Jan S, et al. , GATE V6: a major enhancement of the GATE simulation platform enabling modelling of CT and radiotherapy. Phys Med Biol, 2011. 56(4): p. 881–901. [PubMed: 21248393]
22. Barrett HH, Eskin JD, and Barber HB, Charge transport in arrays of semiconductor gamma-ray detectors. Phys Rev Lett, 1995. 75(1): p. 156–159. [PubMed: 10059139]
23. Jaszczak RJ, et al. , Improved Spect Quantification Using Compensation for Scattered Photons. Journal of Nuclear Medicine, 1984. 25(8): p. 893–900. [PubMed: 6611390]
24. Pourmoghaddas A, et al. , Scatter correction improves concordance in SPECT MPI with a dedicated cardiac SPECT solid-state camera. Journal of Nuclear Cardiology, 2015. 22(2): p. 334–343. [PubMed: 25342215]
25. Suzuki A, et al. , Monte Carlo-based scatter correction considering the tailing effect of a CdTe detector for dual-isotope brain SPECT imaging. Biomedical Physics & Engineering Express, 2016. 2(4).
26. NEMA Standards Publication NU 1–2018: Performance Measurements of Gamma Cameras. 2019: National Electrical Manufacturers Association.
27. Kennedy JA, et al. , Digital Solid-State SPECT/CT Quantitation of Absolute (177)Lu Radiotracer Concentration: *In Vivo* and *In Vitro* Validation. J Nucl Med, 2020. 61(9): p. 1381–1387. [PubMed: 32111686]
28. Shepp LA and Vardi Y, Maximum likelihood reconstruction for emission tomography. IEEE Trans Med Imaging, 1982. 1(2): p. 113–22. [PubMed: 18238264]
29. Thielemans K, et al. , STIR: software for tomographic image reconstruction release 2. Phys Med Biol, 2012. 57(4): p. 867–83. [PubMed: 22290410]

30. Fuster BM, et al. , Integration of advanced 3D SPECT modeling into the open-source STIR framework. Medical physics, 2013. 40(9): p. 092502. [PubMed: 24007178]

31. Huizing DMV, et al. , (177) Lutetium SPECT/CT: Evaluation of collimator, photopeak and scatter correction. J Appl Clin Med Phys, 2020. 21(9): p. 272–277.

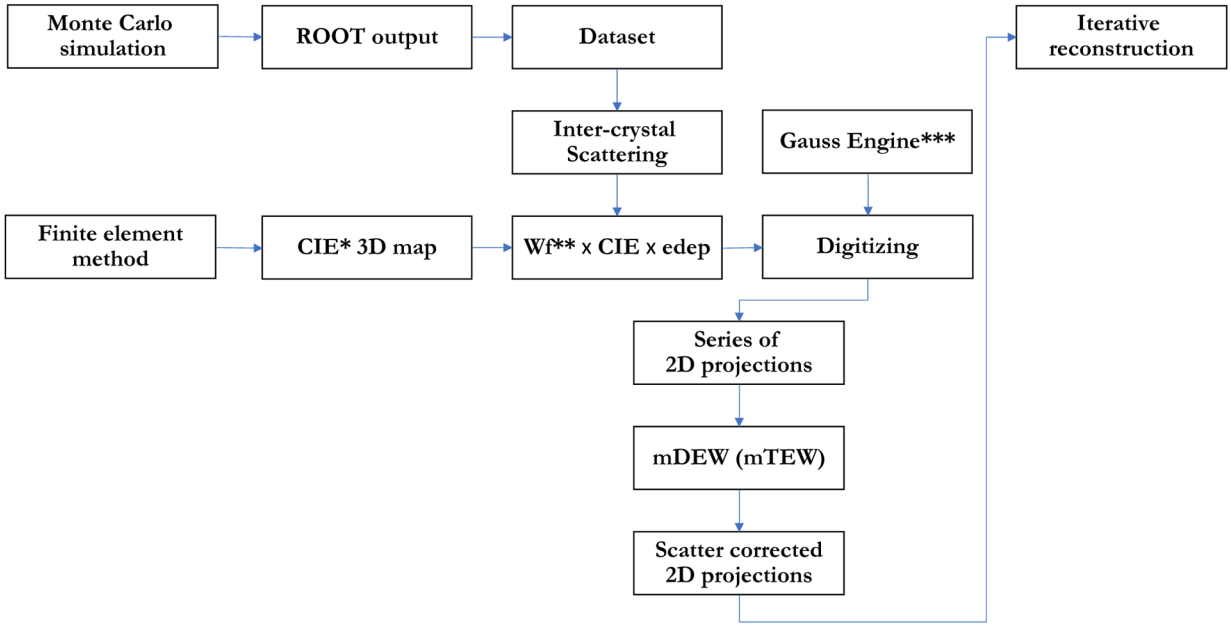

Figure 1.

Diagram summary of our approach. The GATE simulation and the FEM model are used to produce the SPECT projections that are further scatter-corrected and finally reconstructed to yield the final tomographic image of the phantoms.

*Charge induction efficiency. **Weighting factor. ***Referenced from GATE

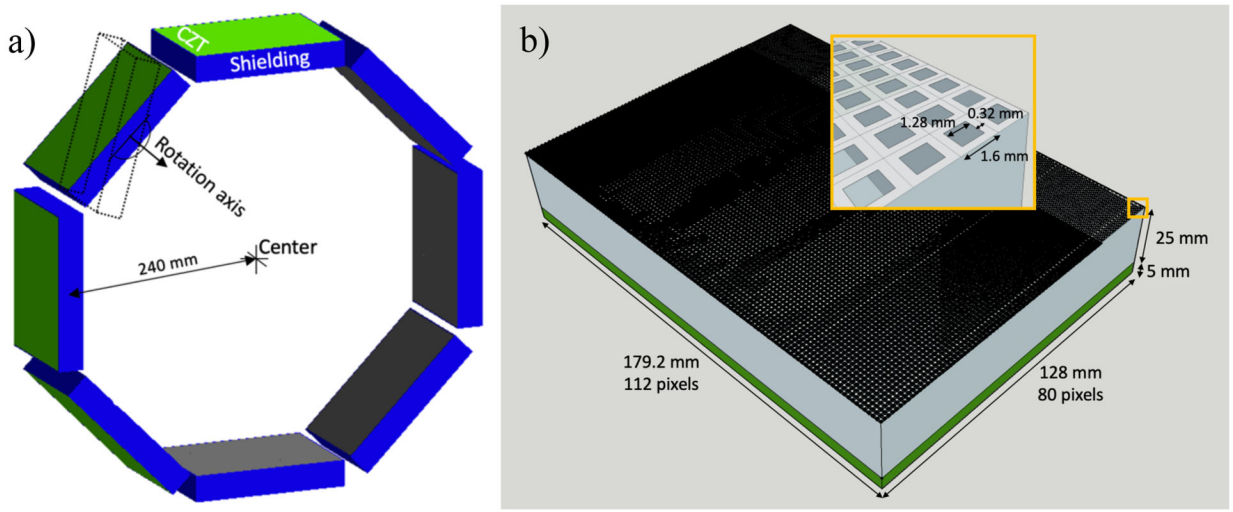

Figure 2.

a) System geometry as simulated in GATE, **b)** close-up of single detector head without shielding.

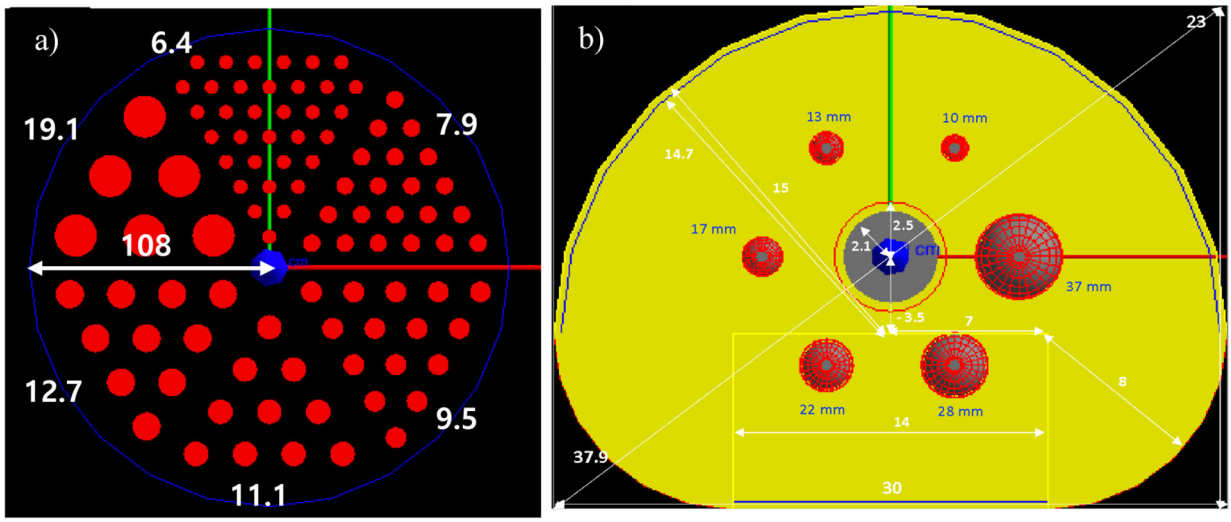

Figure 3.

a) Derenzo phantom seen from the front with the rods marked in red and with the number corresponding to their diameters in millimeters. **b)** NEMA IQ phantom seen from the front. The spheres are highlighted in red and labeled by their diameters, and the warm background is in yellow.

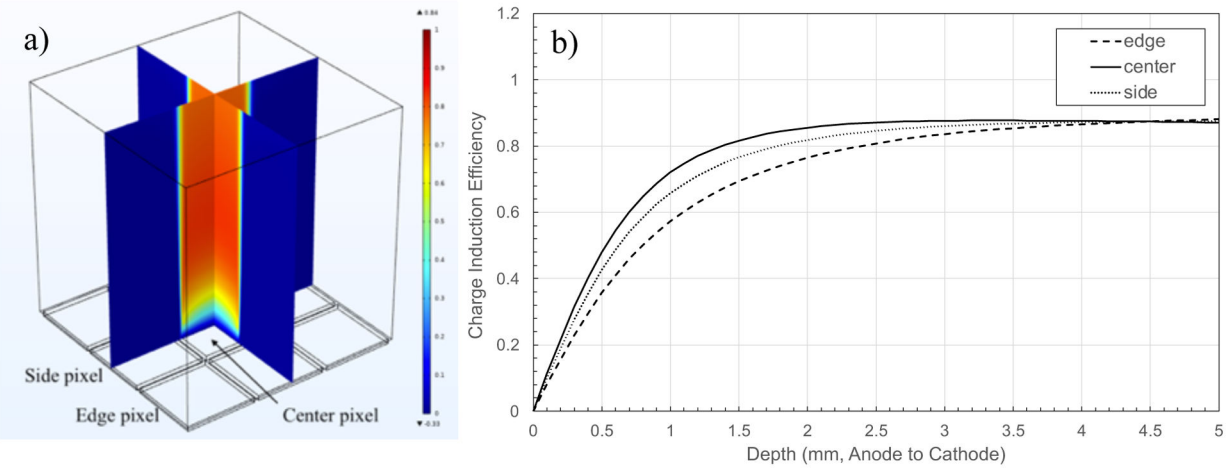

Figure 4.

Central slice of the CIE map obtained from COMSOL for the central pixel **(a)**. CIE as a function of interaction position depth for the center, edge, and side pixels at a fixed voltage of −500V **(b)**. All the curves are averaged over the X and Y dimensions.

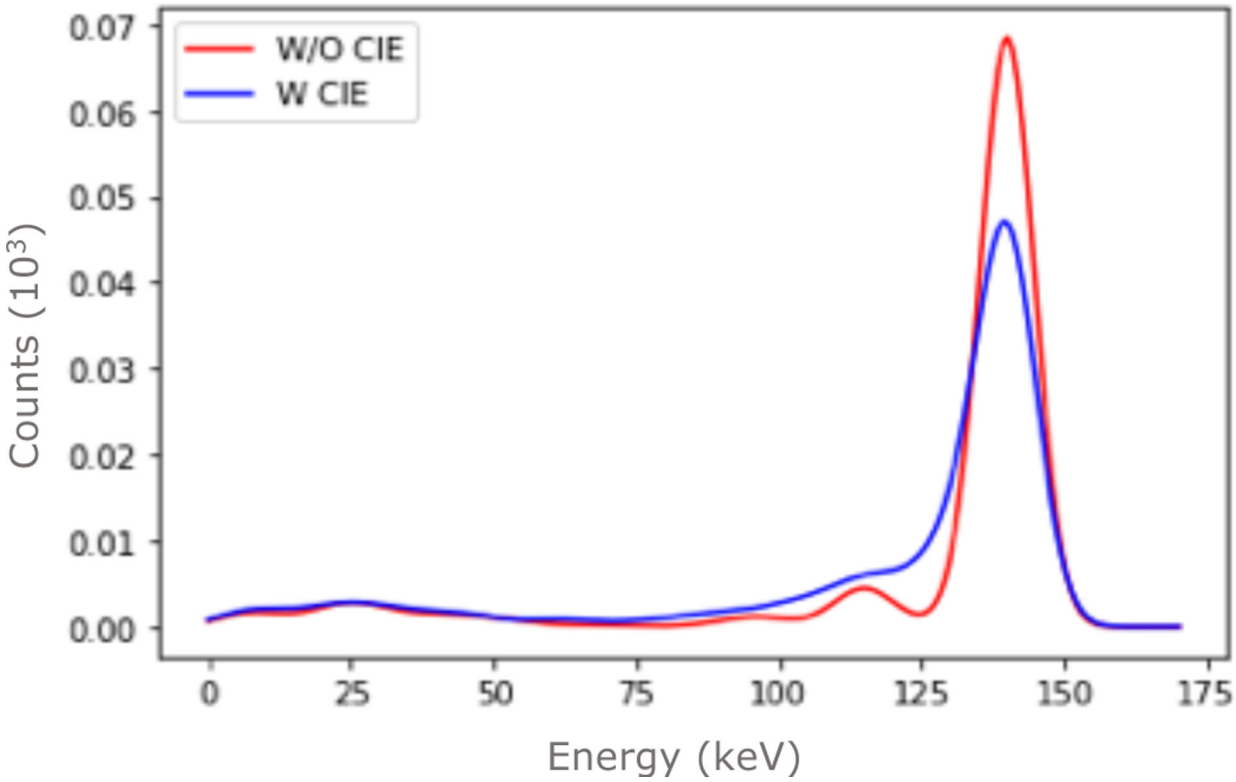

Figure 5.
Energy spectra of a ^{99m}Tc point source in air with (blue) and without CIE (red). The detector model used in our analyses corresponds to the one with CIE (blue).

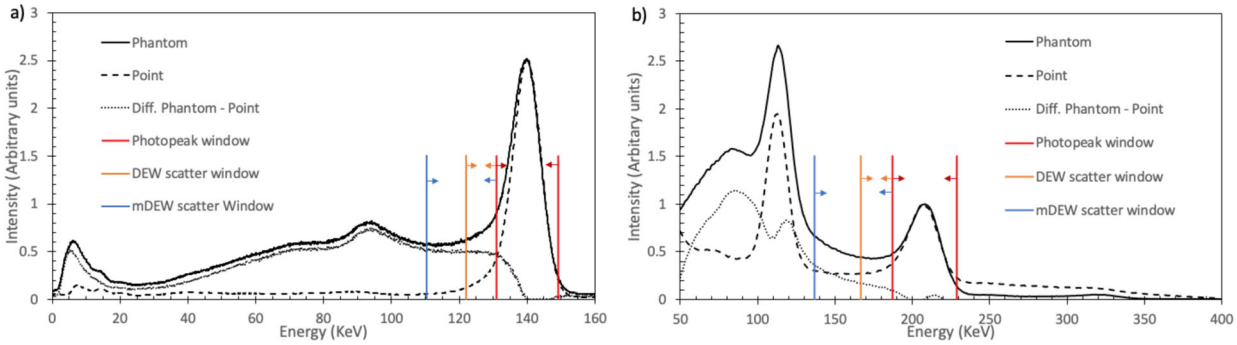

Figure 6.

Energy spectra obtained for a point source and the NEMA IQ phantom for ^{99m}Tc **(a)** and 177Lu **(b)**, used to calculate the parameters k_m and m for the mDEW scatter correction. The energy windows of mDEW are highlighted.

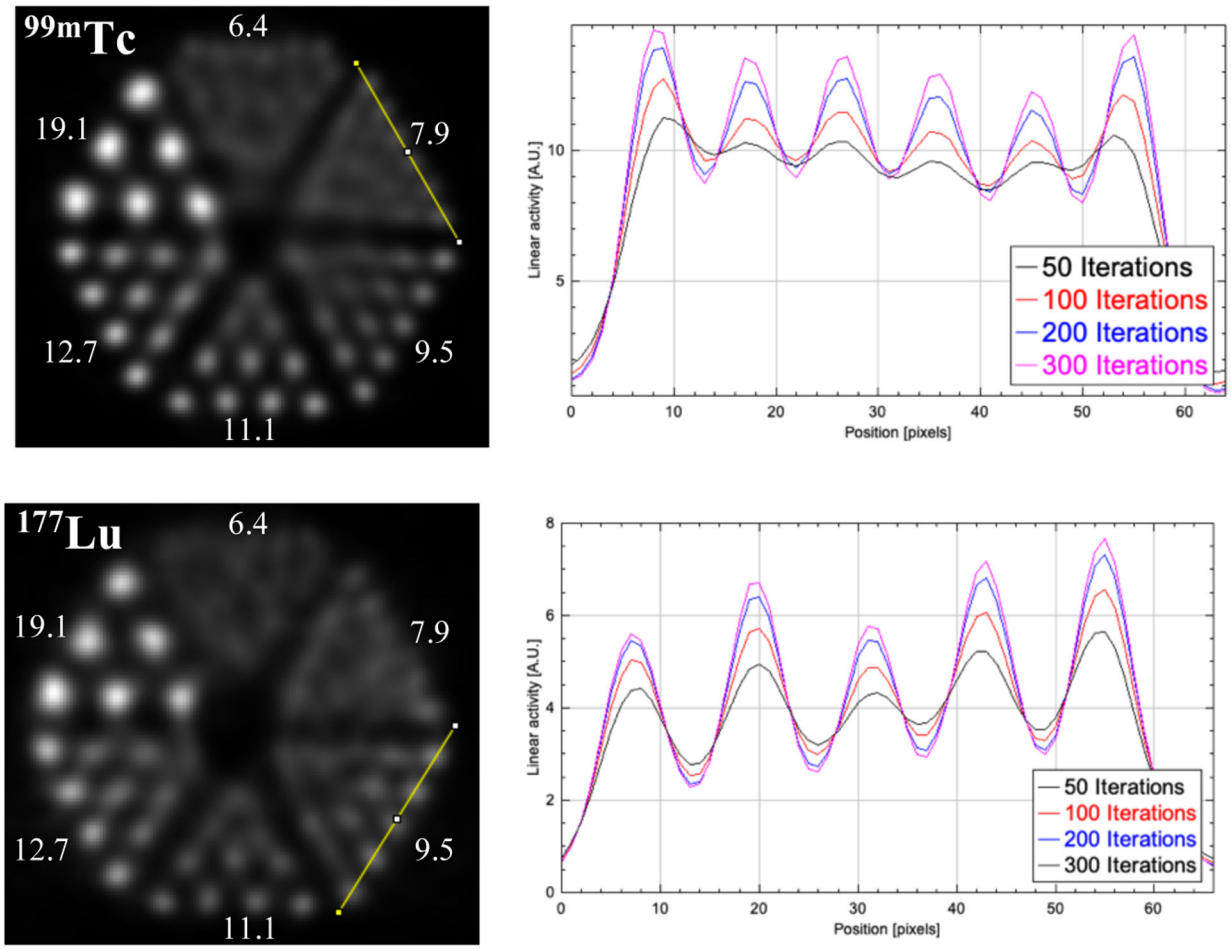

Figure 7.

Axial reconstructed images **(left)** and profiles corresponding to the yellow line **(right)** of the hot-rod Derenzo phantom for ^{99m}Tc **(top)** and ^{177}Lu **(bottom)**. The numbers indicate the diameter of each rod in millimeters.

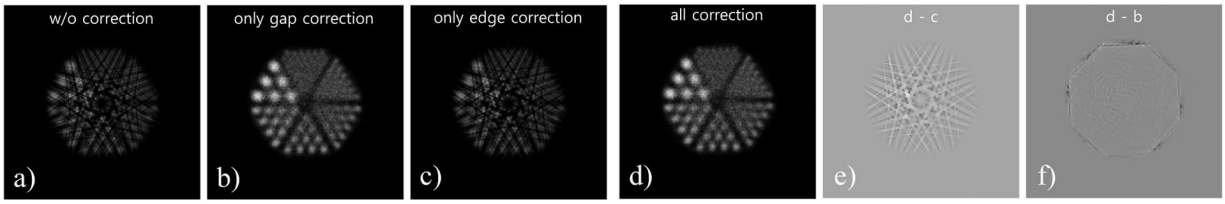

Figure 8.

Axial image of a ^{99m}Tc hot-rod phantom without corrections (a), with only gap correction (b), with only edge correction (c), and with all corrections (d). To better show the effect of the gap and edge corrections, these images do not have attenuation, collimator, detector response or scatter corrections applied. The difference between the fully corrected image and the edge-corrected image (e) and the fully corrected image and the gap-corrected image (f) are also shown.

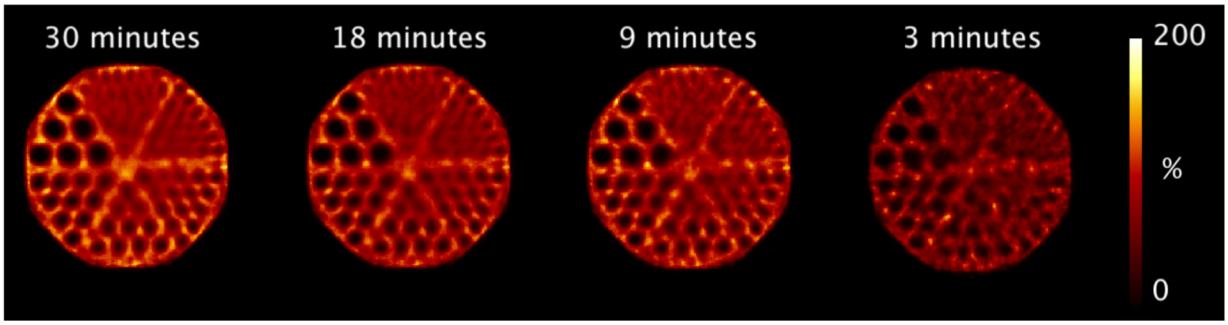

Figure 9.
Transaxial slices of the ^{99m}Tc cold-rod Derenzo phantom for different exposure times. The color scale represents the relative value with respect to the maximum.

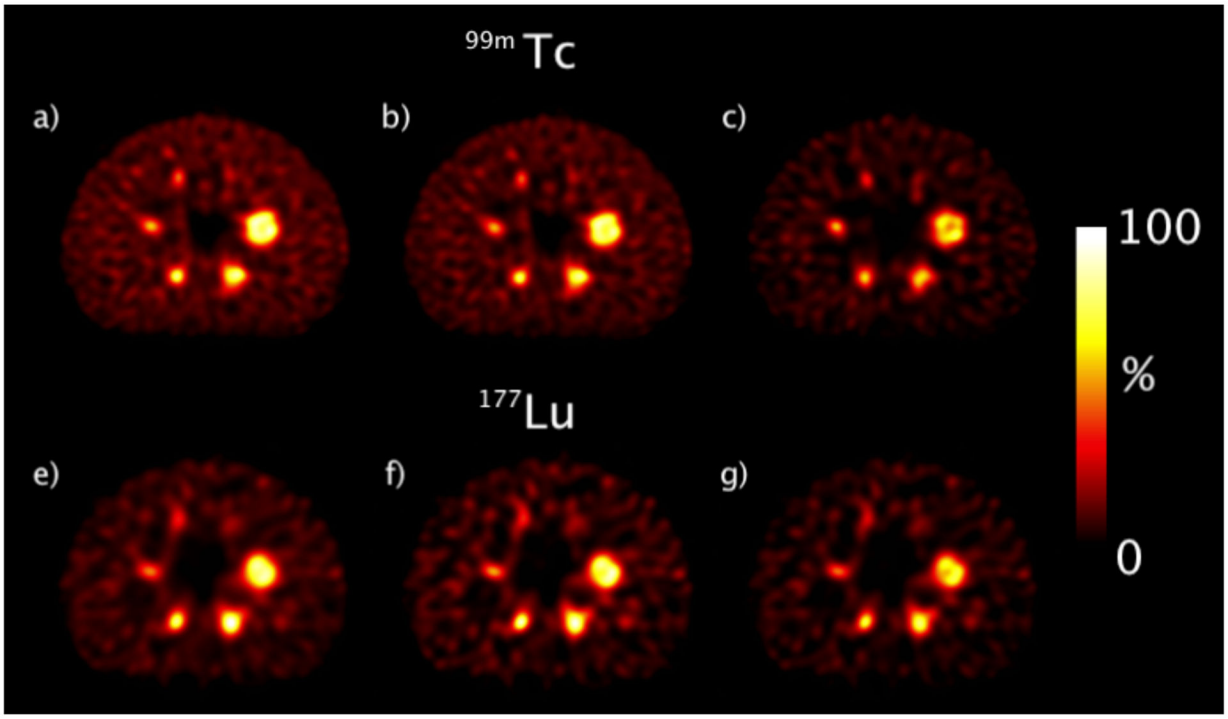

Figure 10.

Central slice of the reconstructed images of the NEMA IQ phantom with ^{99m}Tc at the top and ^{177}Lu at the bottom. From left to right: no DEW scatter correction (a,e), with DEW scatter correction (b,f), and with mDEW scatter correction (c,g). The color scale represents the relative value with respect to the maximum.

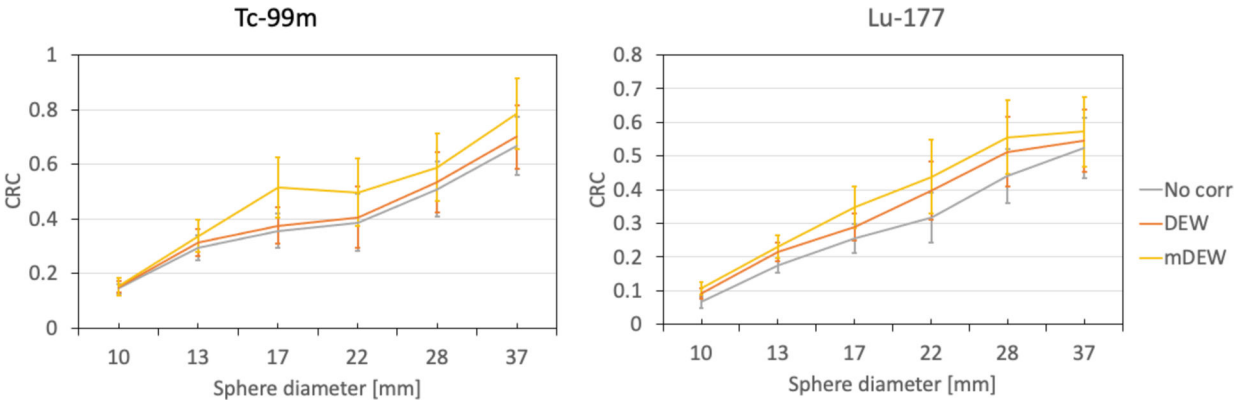

Figure 11.

Contrast recovery coefficient for the NEMA IQ phantom as a function of sphere diameter compared between scatter correction cases for ^{99m}Tc **(left)** and ^{177}Lu **(right)**.

Table I.

Specifications of our CZT-SPECT design for whole-body imaging compared to VERITON [5]. Some parameters for VERITON are not published.

	Parameter	Our design	VERITON
Detector	Number of detector heads	8	12
	Detector heads radial position	185 mm for brain 240 mm for torso (this work)	Variable
	Detector material	CZT	CZT
	Detector thickness	5 mm	-
	Detector head size	179.2 mm × 128 mm	40 mm × 315 mm
	Full detector area	1833 cm^2	1512 cm^2
	Pixel pitch	1.6 mm	2.46 mm
	Number of pixels per head	112 × 80	16 × 128
Collimator	Collimator hole shape	Rectangular	Rectangular
	Collimator material	Tungsten-Alloy W 91%, Ni 6%, Pb 3%	Tungsten-Alloy
	Collimator density	17.3g/cm^3	-
	Collimator length	25 mm	-
	Collimator hole size	1.28 mm	~1mm (4-holes per pixel [15])
	Septal thickness	0.32 mm	~0.2mm [15]
	Shielding material	Same than collimator	-
	Shielding thickness	1.5 mm	-
Imaging	Step angle	5°	-
	Number of steps	18	-
	Time exposure per step	10s for Derenzo - 20s for NEMA	-
	Total acquisition time	3 to 30 minutes	5 to 30 minutes
	^{99m}Tc photopeak energy window	6%	20%
	^{177}Lu photopeak energy window	10%	-

Table II.

Specifications of CZT material for the finite element model

Average atomic number	49.1
Density	5.78 g/cm^3
Electron mobility	1000 cm^2/V/s
Electron lifetime	3×10^{-6} (s)
Hole mobility	50 ~ 80 (cm^2/Vs)
Hole lifetime	10^{-6} (s)
Dielectric constant	10.9
Resistivity	3×10^{10} (cm)
Nominal bias voltage	−500V
Plating material (anode and cathode)	Au

Table III.

Sensitivities calculated with a point source at the center and a hot-rod Derenzo phantom.

Sensitivity [count/s/MBq]	**^{99m}Tc**		**^{177}Lu (208 keV)**	
	S	***S'***	***S***	***S'***
Point source	516.5 ± 5.3	425.0 ± 4.9	43.13 ± 0.5	30.4 ± 0.4
Hot-rod Derenzo phantom	421.6 ± 1.1	170.5 ± 0.7	40.5 ± 1.1	14.0 ± 0.7